The Astrophysical Journal, 713:1310–1321, 2010 April 20 doi:10.1088/0004-637X/713/2/1310

THREE-DIMENSIONAL VIEW OF TRANSIENT HORIZONTAL MAGNETIC FIELDS IN THE PHOTOSPHERE

Ryohko Ishikawa[1,2], Saku Tsuneta[2], and Jan Jurčák[3]
[1] Department of Astronomy, University of Tokyo, Hongo, Bunkyo-ku, Tokyo 113-0033, Japan; ryoko.ishikawa@nao.ac.jp
[2] National Astronomical Observatory of Japan, 2-21-1 Osawa, Mitaka, Tokyo 181-8588, Japan
[3] Astronomical Institute of the Academy of Sciences, Fričova 298, 25165 Ondřejov, Czech Republic
Received 2009 July 26; accepted 2010 February 22; published 2010 April 5

ABSTRACT

We infer the three-dimensional magnetic structure of a transient horizontal magnetic field (THMF) during its evolution through the photosphere using SIRGAUS inversion code. The SIRGAUS code is a modified version of SIR (Stokes Inversion based on Response function), and allows for retrieval of information on the magnetic and thermodynamic parameters of the flux tube embedded in the atmosphere from the observed Stokes profiles. Spectropolarimetric observations of the quiet Sun at the disk center were performed with the Solar Optical Telescope on board *Hinode* with Fe I 630.2 nm lines. Using repetitive scans with a cadence of 130 s, we first detect the horizontal field that appears inside a granule, near its edge. On the second scan, vertical fields with positive and negative polarities appear at both ends of the horizontal field. Then, the horizontal field disappears leaving the bipolar vertical magnetic fields. The results from the inversion of the Stokes spectra clearly point to the existence of a flux tube with magnetic field strength of ∼400 G rising through the line-forming layer of the Fe I 630.2 nm lines. The flux tube is located at around $\log \tau_{500} \sim 0$ at $\Delta t = 0$ s and around $\log \tau_{500} \sim -1.7$ at $\Delta t = 130$ s. At $\Delta t = 260$ s, the horizontal part is already above the line-forming region of the analyzed lines. The observed Doppler velocity is maximally 3 km s^{-1}, consistent with the upward motion of the structure as retrieved from the SIRGAUS code. The vertical size of the tube is smaller than the thickness of the line-forming layer. The THMF has a clear Ω-shaped loop structure with the apex located near the edge of a granular cell. The magnetic flux carried by this THMF is estimated to be 3.1×10^{17} Mx.

Key words: magnetic fields – Sun: granulation – Sun: photosphere – Sun: surface magnetism

1. INTRODUCTION

The Solar Optical Telescope (SOT) spectropolarimeter (SP; Tsuneta et al. 2008a; Suematsu et al. 2008; Ichimoto et al. 2008; Shimizu et al. 2008) on board *Hinode* (Kosugi et al. 2007) revealed that there are ubiquitous horizontally inclined magnetic fields with strengths of a few hundred G in the internetwork regions (Orozco Suárez et al. 2007a; Lites et al. 2008). Centeno et al. (2007) and Ishikawa et al. (2008) reported the temporal evolution of such horizontal magnetic fields both in the quiet Sun and in plage regions. The evolution commonly starts with the appearance of linear polarization signals (horizontal fields) inside granular cells, followed by the appearance of the opposite-polarity circular polarization signals (vertical fields) at both ends of the horizontal component. The time evolution indicates that the horizontally inclined magnetic fields are part of a small magnetic loop. The sizes of the horizontal magnetic fields are smaller than the size of the granule where they appear. Statistical analyses of a large number of the horizontal fields indicate that the lifetime of the horizontal magnetic fields ranges from 1 to 10 minutes and the mean lifetime is about 4 minutes (Ishikawa & Tsuneta 2009a, 2009b). Their occurrence rate is high, and more than approximately 10% of the granules have embedded horizontal magnetic fields (Ishikawa et al. 2008). The movie of linear polarization signals (Ishikawa & Tsuneta 2009a) shows that these horizontal magnetic fields are highly frequent and transient, and the term "transient horizontal magnetic fields" (THMFs) is used for them. Earlier reports of flux emergence in the quiet Sun (Lites et al. 1996; De Pontieu 2002; Martínez González et al. 2007) appear to be examples of THMFs.

The properties of the THMFs described above are the same in the quiet Sun and in the plage region. There are granular-sized horizontal fields in the polar regions, and these magnetic fields may be the same as THMFs (Tsuneta et al. 2008b; Ito et al. 2010). However, there seem to be a few distinct patterns in their disappearance. For example, Ishikawa et al. (2008) report an example of a THMF disappearing in the intergranular lane, while Centeno et al. (2007) show a THMF which disappears inside a bright granule. This is confirmed by Ishikawa & Tsuneta (2009b) who report that normalized continuum intensities where THMFs appear are above ∼1.0, corresponding to the bright granular regions. However, the normalized continuum intensities where THMFs disappear are both higher and lower than ∼1.0, i.e., THMFs do not necessarily reach the intergranular lanes. There also appear to be two types of THMFs; with or without apparent bipolar vertical fields after their disappearance. This variety of THMF behavior suggests a few different scenarios with regard to their disappearance. (1) THMFs somehow submerge with the downward convective motion. (2) They become fragmentary due to the convective flow, and their Stokes signals are below the SP detection level. (3) THMFs go through the line formation layer of the Fe I 630.2 nm lines and reach higher atmospheric layers (Martínez González & Bellot Rubio 2009).

Given the ubiquity of THMFs in the solar photosphere, the question of how they appear and disappear in such a short time becomes one of the important issues in solar magneto-hydrodynamics (MHD). A series of sophisticated MHD simulations (e.g., Vögler & Schüssler 2007; Abbett 2007; Schüssler & Vögler 2008; Isobe et al. 2008; Steiner et al. 2008) have been carried out with varieties of initial and boundary conditions. A detailed comparison of the observed properties of THMFs with the numerical simulation results has just begun. It is thus desirable to clarify the structure and evolution of the enigmatic small-scale magnetic fields in the photosphere, and possibly in the chromosphere.

Spectropolarimetric data obtained with the SOT have been analyzed thus far mainly with inversion codes based on a Milne–Eddington atmosphere (e.g., Lites et al. 2008; Orozco Suárez et al. 2007a; Ishikawa & Tsuneta 2009a). Milne–Eddington inversion provides us with various physical parameters (magnetic field vector and Doppler velocity, etc.), which have to be constant throughout the atmosphere (except for the source function), and synthesize only symmetric Stokes profiles. However, the observed Stokes profiles of the horizontal magnetic fields usually have area-asymmetries. Such asymmetric profiles suggest the presence of velocity and magnetic field gradients along the line of sight (LOS; e.g., Solanki & Pahlke 1988; Sanchez Almeida & Lites 1992). Thus, using the Milne–Eddington inversion, physically important information about the small-scale horizontal magnetic fields may be lost.

We are using an inversion code based on the SIR code (Stokes Inversion based on Response function; Ruiz Cobo & del Toro Iniesta 1992, 1994; Del Toro Iniesta & Ruiz Cobo 1996; Del Toro Iniesta 2003). This code allows for the change of atmospheric parameters along the LOS and thus fits the observed asymmetric Stokes profiles. Martínez González et al. (2007) used the SIR code to analyze a snapshot of the magnetic loops using the spectropolarimetric data of 1.56 μm taken with the Tenerife Infrared Polarimeter. However, the used settings of the inversion assumed the plasma parameters to be constant with height in the atmosphere, except in magnetic field inclination and temperature. Recently, Gömöry et al. (2010) studied the temporal evolution of a similar event applying SIR inversions. However, they kept all magnetic parameters constant with height. Thus, these analyses resemble a Milne–Eddington inversion with a realistic temperature distribution. We fully exploit the inversion code without such constraints to analyze the observed Stokes profiles asymmetries and with a better spatial resolution. This allows us to follow the temporal evolution of the stratified atmosphere.

In this paper, we study a THMF event whose properties are similar to those reported by Centeno et al. (2007). We carry out the full Stokes inversion with the SIRGAUS code (Bellot Rubio 2003), which is a modified version of SIR. The SIRGAUS code treats explicitly a magnetic flux tube embedded in the atmosphere with a Gaussian function, and is expected to be more suitable to obtain vertical (LOS) structure of the THMF. Indeed, we successfully identify an isolated flux tube in the photosphere, and track the emergence of the Ω-shaped flux tube through the photosphere. We describe statistical significance of our result in detail. With the clear identification of the upward moving flux tube, we are able to obtain various physical parameters that characterize the flux tube. Such information on the flux tube becomes available for the first time with the use of the SIRGAUS code. We finally discuss the MHD properties of the THMF.

2. OBSERVATIONS AND WAVELENGTH CALIBRATION

A quiet solar region of $4'' \times 76''$ located near the Sun center was observed with a cadence of 130 s using the SOT/SP on 2007 March 10. We obtained the Stokes spectra of the Fe I 630.2 nm lines, whose line formation region is between $\log \tau_{500} \sim 0$ and -2.5 (Cabrera Solana et al. 2005). Each slit position has an exposure time of 4.8 s, and the scanning step is $0\farcs15$. The noise level in the Stokes Q and U signal is $1.2 \times 10^{-3} I_c$ and that in the Stokes V is $1.1 \times 10^{-3} I_c$, where I_c is the continuum intensity. The dark current, the flat field corrections, and the polarimetric calibration were performed using "sp_prep" software.

We extensively analyze the event shown in Figure 1. The horizontal magnetic field appears at the edge of a granule without any vertical magnetic fields ($\Delta t = 0$ s). At $\Delta t = 130$ s (second frame), the size of the horizontal magnetic field becomes larger and the bipolar vertical fields appear at both ends of the horizontal field. At the third frame ($\Delta t = 260$ s), the horizontal field disappears, leaving an isolated pair of bipolar vertical fields. The separation of these two patches increases with time. The lifetime of the horizontal magnetic field is about 4 minutes, and this event has properties in common with those of the THMFs as reported by Ishikawa et al. (2008).

We analyze only the pixels with the Stokes Q or U amplitude 10 times larger than their noise level. Such pixels are shown with the red contours in Figure 1. Pixels shown with the green contours are dominated by the Stokes V signal, and correspond to the footpoints of the THMF. These pixels are also analyzed.

The Doppler velocity information is crucial for understanding the dynamics of the flux tube. For this purpose, accurate in-orbit calibration of the SOT/SP wavelength scale and offset is done to obtain the absolute velocity scale. We here calibrate our data using the solar flux atlas (Beckers et al. 1976). The atlas contains high-resolution spectra of the solar irradiance from 380 nm to 700 nm and has the wavelength information.

First, we obtain the mean Stokes I profile of the quiet Sun by averaging the Stokes I profiles of pixels without the polarization signal. Second, we compare the mean Stokes I profile with the solar flux atlas and derive the wavelength sampling of 2.14 pm and the wavelength value at the start pixel of 630.089 nm. These two parameters give us the maximum correlation coefficient between the mean Stokes I profile obtained with the SOT/SP and the solar flux atlas (see Figure 2). However, the wavelength shift of the flux atlas is not corrected for the gravitational redshift and convective blueshift (Allende Prieto & Garcia Lopez 1998). It turns out that the two Fe I lines have the redshifts of 0.88 pm and 0.63 pm (420 m s^{-1} and 300 m s^{-1}) with respect to the laboratory centers, respectively. These different Doppler shifts come from the difference in the convective blueshifts between the two lines. Thus, we define the mean value of the two redshifts for the two Fe I lines to be 360 m s^{-1} as the zero point of the velocity scale. With this process, we have corrected the effect of the gravitational redshift and the convective blueshift. The Doppler velocities in this paper are now defined such that if there is no motion on the Sun, this will give the zero velocity.

3. SIRGAUS INVERSION

We perform the inversion of the observed Stokes profiles using the SIRGAUS code (Bellot Rubio 2003). This inversion code synthesizes the Stokes profiles emerging from a model atmosphere and then compares them to the observed ones. Using the least-square Levenberg–Marquardt algorithm, the initial model is modified until the difference between the observed and the synthetic profiles is minimized. The model consists of a simple atmosphere that represents the *background* and a Gaussian-shaped bump superposed on some of the atmospheric parameters representing an embedded flux tube. Note that we are considering a one-component model atmosphere. The THMF analyzed here is spread out over several pixels. Therefore, we assume that the magnetic filling factor, f, is 1.

Recent Milne–Eddington inversions of THMFs have provided an average filling factor of about 0.2 (Ishikawa & Tsuneta 2009a). The observed magnetic structures we want to analyze cover more than a spatial resolution element of the SP data. Thus, if we neglect stray-light contamination effects like those

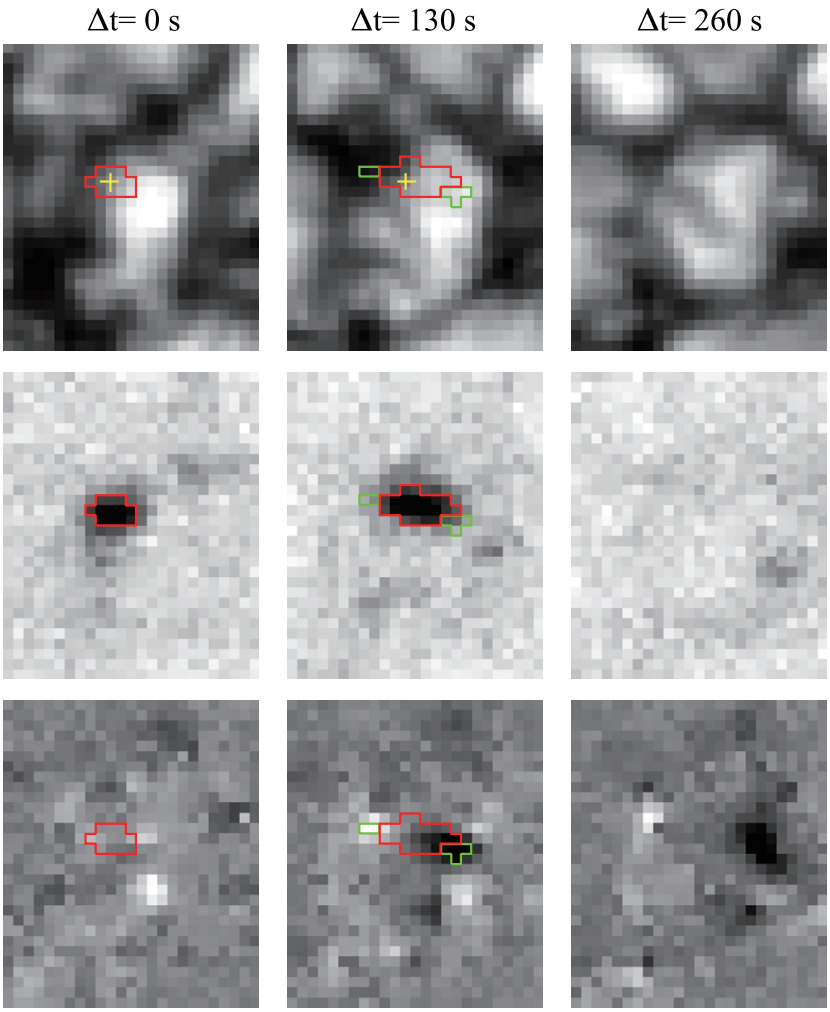

Figure 1. Temporal evolution of the continuum I_c (top) and the integrated linear/circular polarization signal (middle/bottom). The integration range for the linear polarization signal is from −21.4 pm to 21.4 pm from the line center of the Stokes I spectra at each pixel. The integration for the circular polarization is carried out from −21.4 pm to −4.28 pm and from 4.28 pm to 21.4 pm, taking the absolute values of the Stokes V spectra. The sign for the obtained circular polarization signal is determined to be the sign of the peak Stokes V profile at the blue wing. The time cadence is 130 s. The pixels to be analyzed in this paper are shown with red and green contours (see the text).

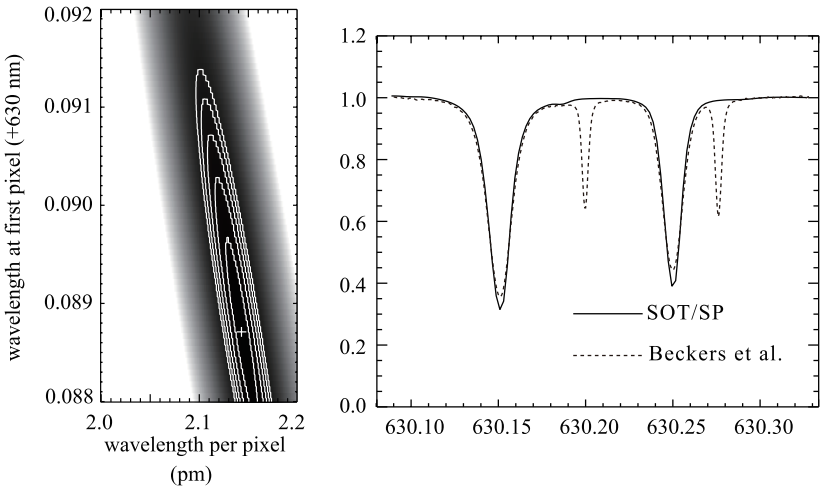

Figure 2. Left: correlation coefficient for the combination of the SOT/SP wavelength per pixel and the wavelength at the first pixel (offset). The contours show the correlation coefficient of 0.929, 0.931, 0.933, 0.935, and 0.937. The cross represents the position with the maximum correlation coefficient of 0.938, in which the wavelength per pixel and the wavelength at the first pixel are 2.14 pm pixel^{-1} and 630.089 nm. Right: the SOT/SP mean Stokes I profile (see the text), which is wavelength-calibrated compared to the solar atlas (Beckers et al. 1976). Note that these profiles are normalized to the continuum intensity.

due to diffraction (Orozco Suárez et al. 2007b) or scattered light, we would expect f to be around unity. The obtained small filling factors might be just a net effect of the used technique that cannot account for a flux tube fully covering the resolution

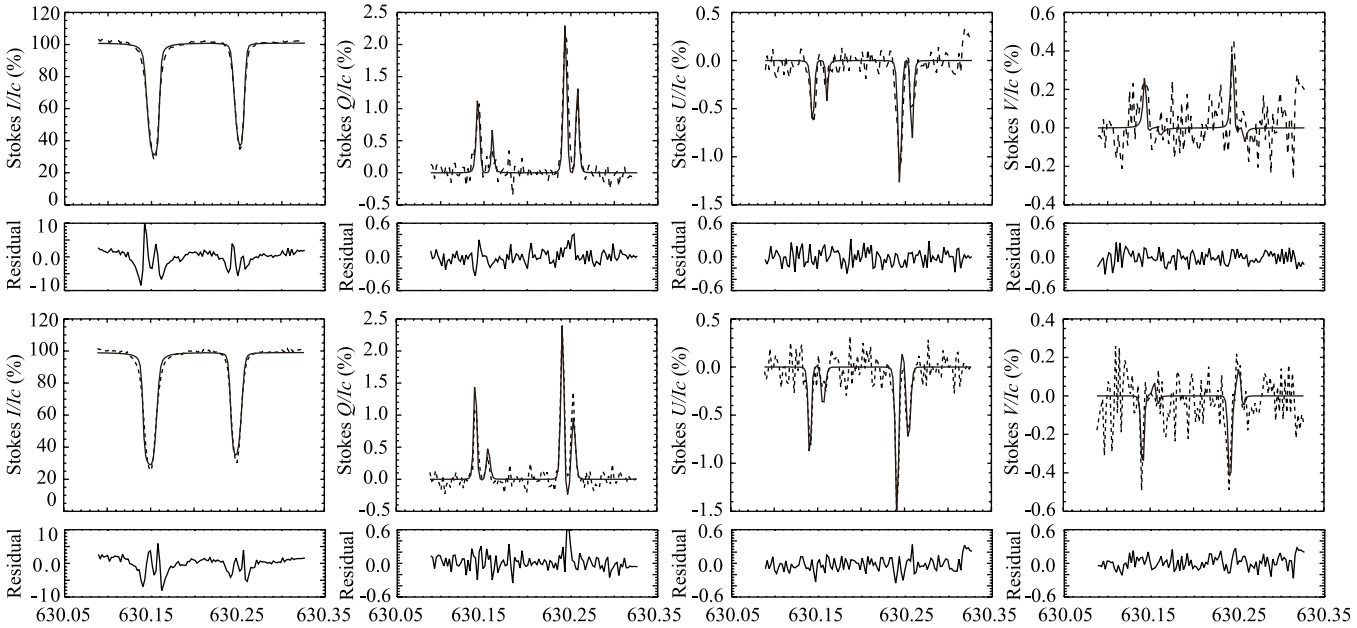

Figure 3. Observed (dashed) and the synthetic (solid) Stokes profiles for pixel 1 from the first scan (top) and pixel 2 from the second scan (bottom). At the bottom of each panel, the difference between the observed and the synthetic profiles is shown in percent.

element, but only partially occupying the line-forming region of the Fe I lines at 630.2 nm.

Thus far, this code has not been widely used. Examples of its application to spectropolarimetric data can be found in, e.g., Jurcák et al. (2007) where they analyze Stokes profiles observed in sunspot penumbrae. As explained before, in SIRGAUS the distribution of the atmospheric parameters, x, consists of a background atmosphere and of a Gaussian bump, and can be written as

$$x(\eta) = x^b(\eta) + \Delta x \exp\left(-\frac{(\eta - G_{\rm pos})^2}{G^2_{\rm width}}\right), \qquad (1)$$

where x^b stands for the background plasma parameters; Δx represents the amplitude of the Gaussian bump; η is the logarithm of the optical depth, τ_{500}; and $G_{\rm width}$ and $G_{\rm pos}$ are the width and the position of the Gaussian bump in η units. The value of the amplitude, Δx, is different for each of the physical quantities. The Gaussian bump position and width are the same for all the physical quantities.

The SIRGAUS code tries to find the best model atmosphere that reproduces the observed profiles in a space of 14 free parameters. The temperature, T, of the background atmosphere is allowed to change at three nodes.[4] The other free parameters, x^b, characterizing the background atmosphere, say the microturbulence, $v^b_{\rm mic}$, the LOS velocity, $v^b_{\rm LOS}$, and the field strength, B^b, its inclination, γ^b, and azimuth, ϕ^b, are assumed to be constant with height. The rest of the free parameters are the amplitudes of the bumps, $\Delta v_{\rm LOS}$, ΔB, $\Delta\gamma$, and $\Delta\phi$, and their width, $G_{\rm width}$, and position, $G_{\rm pos}$. Hereafter and for simplicity, since the Gaussian bump describes the plasma parameters of a flux tube embedded in the line-forming region of the observed spectral lines, the Gaussian bump will be referred to as flux tube.

Throughout this paper, we are displaying the resulting distributions of plasma parameters as a function of the logarithm of the continuum optical depth at 500 nm; $\log\tau_{500}$, hereafter referred to as $\log\tau$. However, the optical depths will be converted to kilometers to specific purposes (see, e.g., Section 6.4). To this end, we solve the following equation: $\tau = \int_0^z \kappa\rho dz$. With the boundary condition $\tau = 1$ at $z = 0$ km, κ is the continuum absorption coefficient per unit mass and ρ is the gas density. The absorption coefficient depends on different plasma parameters and on the chemical composition. The results from the SIRGAUS inversion are used to evaluate the previous equation at each pixel. For its integration, we use the program geometrical.x, provided with the SIR code. The same program also provides us with the values of the gas density that will be used later in this paper (see Section 7.2).

[4] See, e.g., Ruiz Cobo & del Toro Iniesta (1992).

4. EMERGENCE OF HORIZONTAL MAGNETIC FIELDS

In order to clearly show the evolution of the horizontal magnetic field between the two scans, we select two pixels, one in each scan, and present their detailed analysis. The selected pixels are marked by yellow crosses in Figure 1. The corresponding observed Stokes profiles are shown in Figure 3. To invert the Stokes profiles of all pixels, we used several initial atmospheric models. For the pixel taken from the first scan (hereafter pixel 1), all the initial models converged to a solution where the flux tube is located low in the atmosphere. On the other hand, the solutions for the pixel from the second scan (pixel 2) show that the position of the flux tube is located higher in the photosphere.

To show the reliability of the obtained positions and widths of the flux tube, we proceeded as follows. First, we fixed all the plasma parameters obtained by the SIRGAUS inversion. Then, we evaluated a merit function for a wide range of $G_{\rm width}$ and $G_{\rm pos}$ values. For this purpose, we introduced a χ^2 function that does not take into account the contribution of the Stokes I profile:

$$\chi^2 \equiv \sum_{k=1}^{3}\sum_{l=1}^{n} \frac{\left[I_k^{\rm obs}(\lambda_l) - I_k^{\rm syn}(\lambda_l)\right]^2}{\sigma_o^2}, \qquad (2)$$

where n is the number of the wavelength points; I_k with $k = 1, 2, 3$ indicates the Stokes Q, U, and V profiles; $I_k^{\rm obs}$ and $I_k^{\rm syn}$ stand for the observed and the synthetic profiles, respectively;

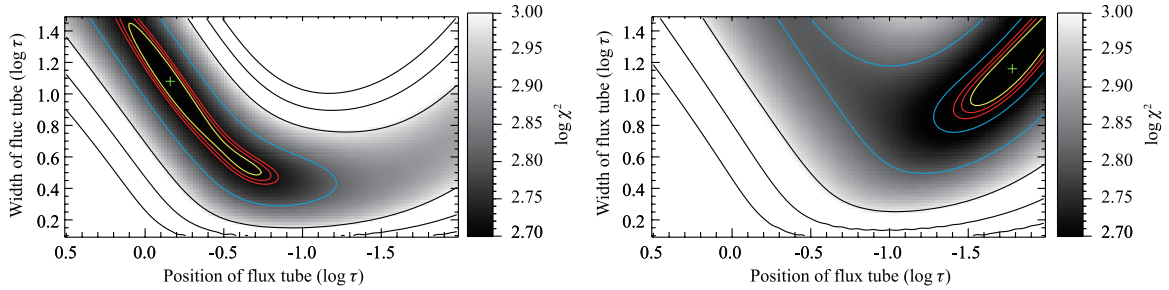

Figure 4. χ^2 maps in the parameter space of the position and width of the flux tube for pixel 1 ($\Delta t = 0$ s, left) and pixel 2 ($\Delta t = 130$ s, right). The cross shows the position where the χ^2 is minimum. The yellow line indicates $\Delta\chi^2 = 13.7$ (1σ) and the red ones $\Delta\chi^2 = 21.3$ (2σ) and 29.8 (3σ). Blue contours indicate the reduced χ^2 values of 1.5 and 2.0, while black ones correspond to 3.0, 4.0, and 5.0. We define the reduced χ^2 as $\chi^2/(3n - p)$, where n is the number of the wavelength points and p the number of free parameters.

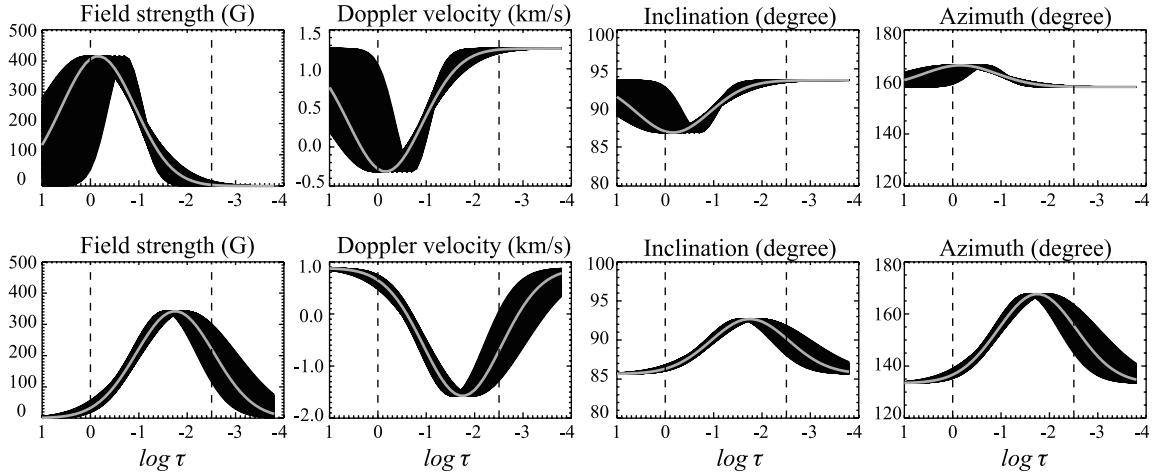

Figure 5. Various physical parameters as a function of the optical depth obtained for pixel 1 (top) and pixel 2 (bottom). The gray lines show the parameters with the smallest χ^2 value. The black areas are created by plotting the distributions of plasma parameters within the 1σ confidence regions. The dashed lines enclose the line-forming region of the Fe I 630.2 nm lines.

and σ_o is the standard deviation of the Stokes Q, U, and V profiles estimated using pixels without any apparent polarization signal. It represents the Poisson noise of incident photons and the value is $\sim 1.1 \times 10^{-3} I_c$ (see Section 2).

Hereafter, we use the χ^2 function as defined in Equation (2). The SIRGAUS code minimizes a χ^2 that takes into account all four Stokes profiles. The synthetic Stokes profiles shown in Figure 3 are example fits to the observations. As can be seen in the lower panels (residuals), the fits are very good for the Q, U, and V profiles and reasonable for the I profile. The largest discrepancies are obtained in the wings of the Stokes I profile with a maximum of about 10%. The origin of the residual error in the wings of Stokes I may be due to not taking into account the hydrogen collisional broadening (L. R. Bellot Rubio 2009, private communication). However, it should be noted that SIRGAUS retrieves the information about the atmospheric structure along the LOS mainly from the asymmetries of the Stokes Q, U, and V profiles. For this reason, we use a χ^2 based only on the Stokes Q, U, and V profiles. This χ^2 definition will also help in clarifying the properties of the flux tube.

Figure 4 shows the dependence of the χ^2 values on the position and width of the flux tube for pixels 1 and 2 (left and right panels, respectively). The minimum values ($\chi^2_{\rm min}$) are marked by the crosses and correspond to the synthetic profiles shown in Figure 3 and to the models shown by the gray lines in Figure 5. To construct Figure 4, we fix 12 of the 14 free parameters and evaluate the χ^2 value using Equation (2) and varying the $G_{\rm pos}$ and $G_{\rm width}$. The solid curves in Figure 4 are defined by constant values of $\Delta\chi^2 \equiv \chi^2 - \chi^2_{\rm min}$. The region outlined by the $\Delta\chi^2$ curves defines the level of confidence: for instance, there is a 68.3% (1σ) chance for the true parameters of the position and width of the flux tube to fall within the region defined by the yellow contour ($\Delta\chi^2 = 13.7$). Likewise, there is 95.4% (2σ) and 99.7% (3σ) chance that the true parameters fall inside the red contours with $\Delta\chi^2 = 21.30$ and 29.8, respectively. As explained before to make Figure 4, we have varied two parameters (the positions and widths of the flux tube) and remaining 12 parameters are fixed. In this case, $\Delta\chi^2$ is distributed as a chi-square distribution with $14-2 = 12$ degrees of freedom (TheoremD in Press et al. 2007). The $\Delta\chi^2 = 13.7$, 21.3, and 29.8 used above come from the chi-square distribution function for 12 degrees of freedom and for the confidence level of 68.27%, 95.45%, and 99.73%, respectively.

In pixel 1 ($\Delta t = 0$ s), the χ^2 is minimum when the position of the flux tube is about $\log\tau \sim -0.15$ and its width is about 1.1. However, these parameters are not determined uniquely since the 1σ confidence level is elongated. The positions of the flux tube extend from $\log\tau \sim 0.1$ to -0.7 with $G_{\rm width}$ changing accordingly from 1.4 to 0.5. A thick flux tube located deeper in the photosphere and a thin flux tube located higher in the atmosphere provide equally good fits to the observed spectra. From these results, we can ascertain that the center of the flux tube is not located higher than $\log\tau \sim -0.7$. This optical depth corresponds to a geometrical height of 91 km.

The 1σ confidence level is less elongated for pixel 2 ($\Delta t = 130$ s), but again, it is difficult to specify the exact width and

position of the flux tube. The minimum χ^2 is obtained when the position of the flux tube is about $\log\tau \sim -1.8$ and its width is about 1.1. The position of the flux tube is definitely higher than $\log\tau \sim -1.5$, i.e., 213 km. In conclusion, the χ^2 maps clearly show with sufficient statistical significance that the magnetic flux tube is located higher in the atmosphere at $\Delta t = 130$ s than at $\Delta t = 0$ s. Therefore, the flux tube moves upwards with time.

The distributions of plasma parameters as a function of the optical depth are shown in Figure 5. The gray line stands for the atmospheric model at $\chi^2_{\rm min}$. The black areas represent the variation within the 1σ confidence region. We first note that the flux tube does not occupy the whole line-forming region. For pixel 1, the center of the flux tube is around $\log\tau \sim -0.5$ and we are observing the upper boundary of the flux tube. On the other hand, for pixel 2, the flux tube is located at around $\log\tau \sim -1.7$ and the lower boundary of the flux tube is observed. For both pixels, the background plasma is not magnetized even though we allow the field strength to change in the inversion. Thus, the flux tube is located in an essentially field-free atmosphere.

The plasma parameters such as the magnetic field strength significantly change as a function of the optical depth in the line-forming region due to the presence of the flux tube (Figure 5). The large gradients are probably responsible for the observed asymmetries of the Stokes profiles. We note that the variation in the plasma parameters (as represented by the black areas in Figure 5) at the same optical depth is relatively small, regardless of the considerable differences in the widths and the positions of the flux tube, essentially within the line-forming regions (the region delimited by the two dashed lines in Figure 5). For pixel 1, the values above $\log\tau \sim 0$ are similar: the broader the flux tube becomes, the deeper it is located to maintain the similarity in the distribution. Likewise, pixel 2 has a similar situation. The values of the plasma parameters are similar at the same optical depth below $\log\tau \sim -2.0$, regardless of the widths and the positions of the flux tube. Broader flux tubes are positioned higher in the atmosphere for the same reason.

The rising motion of the flux tube is confirmed by the distributions of LOS velocity. The LOS velocity distributions shown in Figure 5 indicate that the flux tube is slightly blueshifted below $\log\tau = -0.7$ for pixel 1. The velocity of the flux tube shows an upward motion with respect to the background atmosphere at $\log\tau \sim -1.5$. The relative velocity of the flux tube is $\sim$1.3 km s^{-1}. For pixel 2, the flux tube is blueshifted, showing LOS velocities up to 1.6 km s^{-1}. The relative velocity with respect to the background is larger than for pixel 1.

As can be seen in Figure 5, the inclination angle of the flux tube is $\sim$90°, so that the field lines are perpendicular to the LOS for both pixels. The azimuth angle, measured from the east–west direction, is about 160°, indicating that the field lines are nearly parallel to the line connecting the negative and positive Stokes V patches of the second scan. The magnetic field strengths are around 400 G in both cases.

5. THREE-DIMENSIONAL STRUCTURE AND TIME EVOLUTION

We have analyzed those pixels outlined by red and green contours (see Figure 1), following the approach we applied to pixels 1 and 2 in the previous section. Figures 6 and 7 show the corresponding χ^2 maps for these pixels. Pixels 1 and 2 correspond to pixel 1–6 in Figure 6 and pixel 2–14 in Figure 7, respectively.

In the first scan, the results are comparable to those found for pixel 1. The 1σ confidence regions are elongated and located low in the atmosphere. However, this is not the case for pixels 1–1 and 1–4. In these pixels, although the fits are as good as those in the neighboring pixels, the location of the flux tube is different.

In the center of the THMF (pixels 1–6 and 1–2), the 1σ confidence region is located between $\log\tau = 0$ and $\log\tau = -0.7$. There, the position of the flux tube is the highest. In the surrounding pixels (1–3, 1–5, 1–7, 1–9, 1–10, and 1–11), the 1σ confidence region is located below $\log\tau \sim 0$. At the one of edges of the THMF (pixels 1–8 and 1–12), the location of the flux tube is even lower. In summary, if we go from the center of the THMF to any of its edges, the flux tube sinks into the photosphere. Note that for most pixels the lower boundary of the flux tube is below the continuum formation level. This result is compatible with the presence of a low-laying flux tube with an Ω shape. Only the apex of the flux tube is detected in linear polarization (i.e., horizontal fields) and therefore, the footpoints of the loop are not seen.

In the second scan, in the center of the THMF, the flux tube is located at around $\log\tau = -1.6$. When we go from the center of the THMF toward any of its footpoints (e.g., from pixels 2–15 to 2–19), the flux tube is located deeper in the atmosphere. Again, this is consistent with a flux tube with an Ω shape. The retrieved shape and position of the flux tube from the first and second scan confirm our observation of a rising Ω loop.

6. PROPERTIES OF THMF

6.1. Magnetic Field Topology

The lower left part of Figures 6 and 7 shows the azimuth angles of the magnetic field lines retrieved with the SIRGAUS code at $\log\tau = -1.0$. For both scans, the magnetic field is aligned with the axis of the flux tube, i.e., with the line connecting the opposite polarity patches. The averaged azimuth angles around the center of the THMF are 164° and 162° for the first and second scan, respectively. Since the azimuth is displayed at the same optical depth for both scans, it means that the direction of magnetic field is the same in the upper part of the flux tube observed at $\Delta t = 0$ s as in the lower part of the flux tube observed at $\Delta t = 130$ s. This indicates that the analyzed THMF does not show any helical structure, so that essentially, the flux tube has a toroidal component only.

The pixels in which the azimuthal directions are shown with green lines in Figures 6 and 7 are selected for plotting the magnetic field strength cross section of the flux tube, along its axis (top panels in Figure 8). Left and right panels correspond to the first and second scans. For both scans, the field strength distributions clearly show that the flux tube is located deeper in the atmosphere, going from the center to the edge of the THMF. In the first scan, we detect only the apex of the flux tube, while in the second scan the flux tube is already located high in the line-forming region. These results clearly indicate a rising Ω-shaped flux tube. The magnetic field strength of the flux tube is smaller than 400 G. We do not see any change in magnetic field strength between the first and second scan.

The white lines plotted over the distributions of the magnetic field strength in Figure 8 mark its inclination. In the first scan, only the horizontal component of the magnetic field can be detected, $\gamma \sim 90°$, (there is no Stokes V signal observed during this scan). The inclination at the central part of the THMF is also around 90° in the second scan. However, near the region where

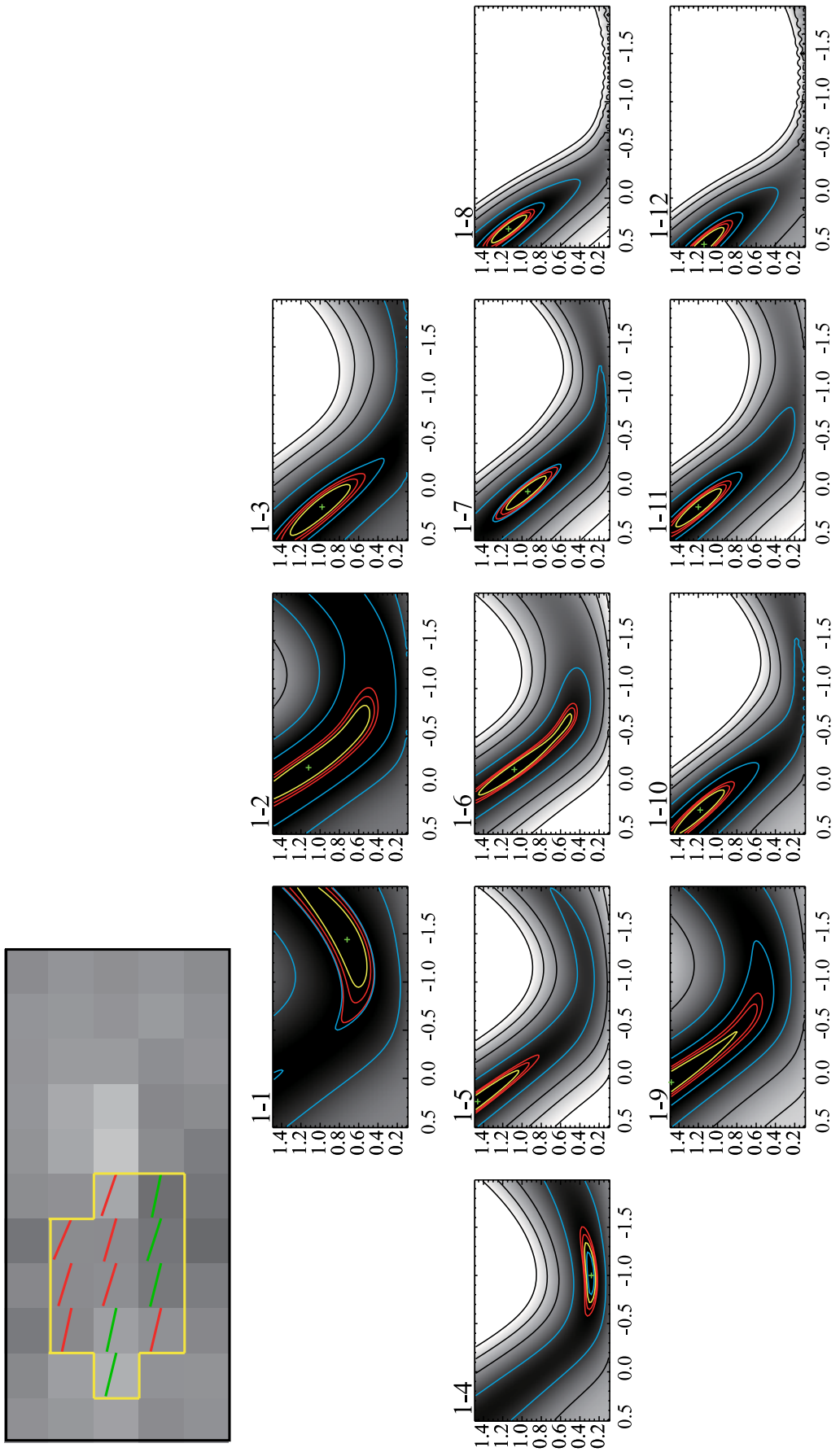

Figure 6. χ^2 maps equivalent to those shown in Figure 4 for the first scan ($\Delta t = 0$ s). Pixel 1–6 corresponds to pixel 1. Lower left panel shows the integrated circular polarization signals for these pixels. The green and red lines represent the azimuth direction at $\log \tau = -1$.

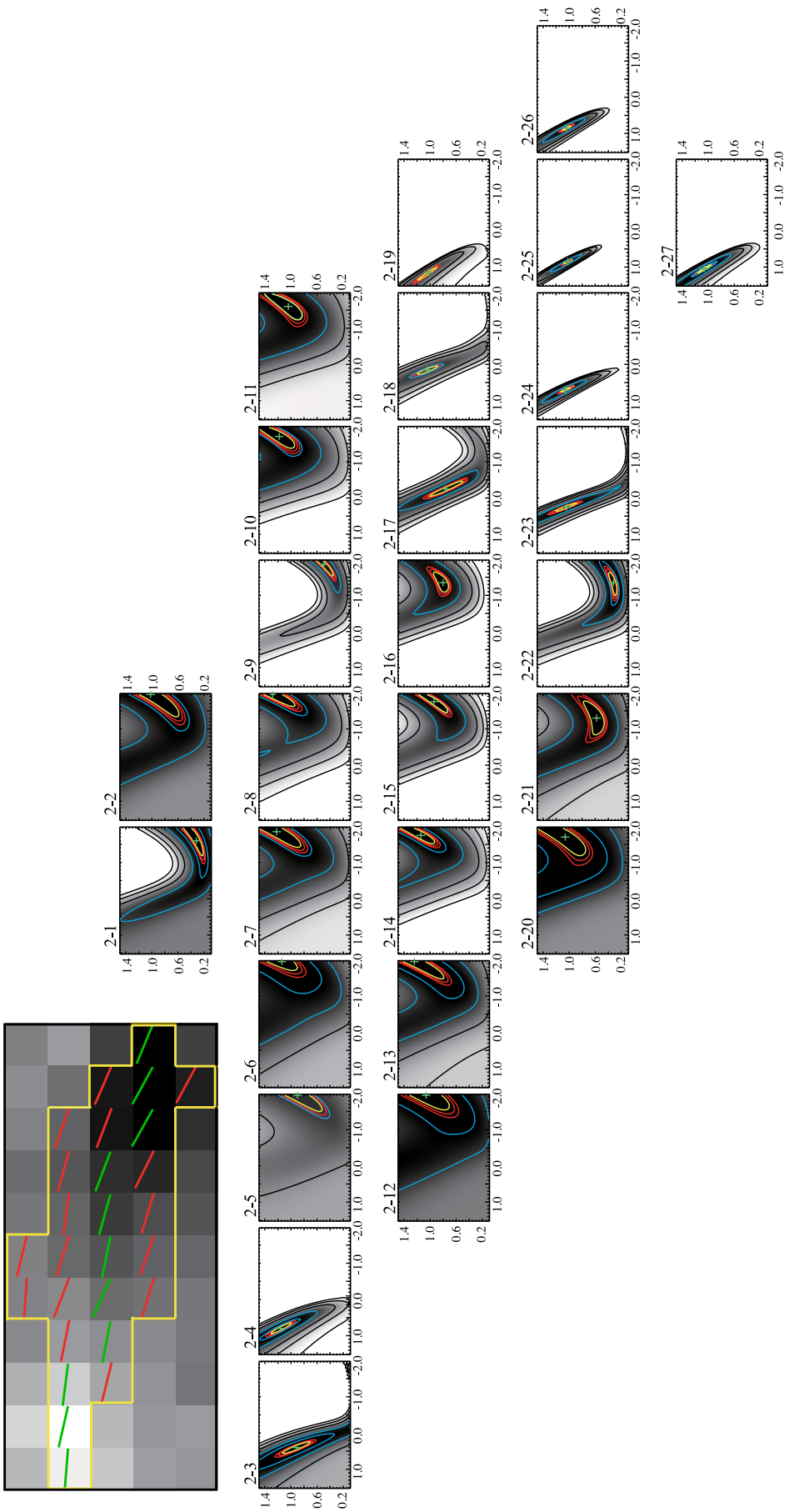

Figure 7. Same as Figure 6, but for the second scan ($\Delta t = 130$ s). Pixel 2–14 corresponds to pixel 2.

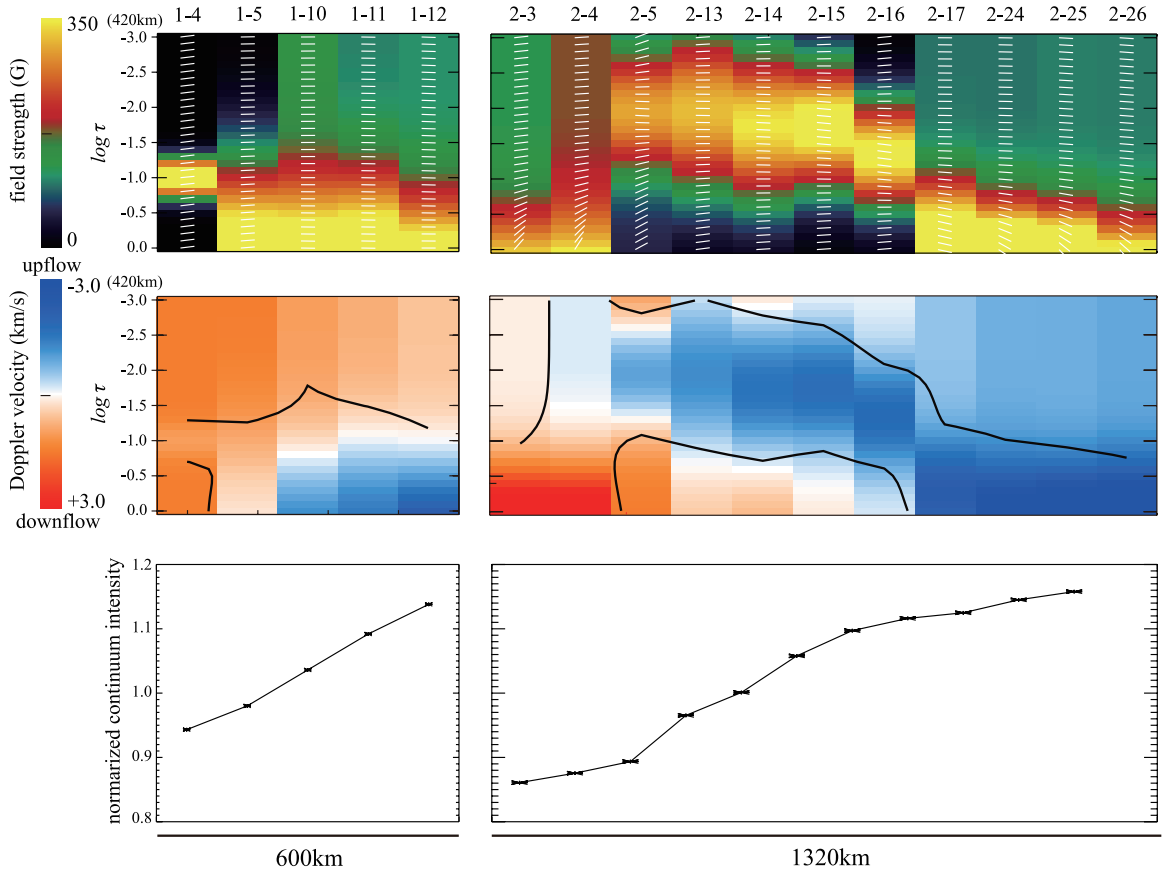

Figure 8. Top panels: cross-sectional view of the magnetic field strength of the THMF for the first (left) and the second (right) scans. White lines show the inclination of the magnetic field vector. Middle panels: cross-sectional view of the Doppler velocity. The region with field strength above 150 G is contained with the solid lines. The shown distributions correspond to the pixels that are indicated by green lines in the azimuth maps from Figures 6 and 7. For each pixel, the atmospheric parameters with the minimum χ^2 are plotted. The bottom two panels represent the normalized continuum intensity.

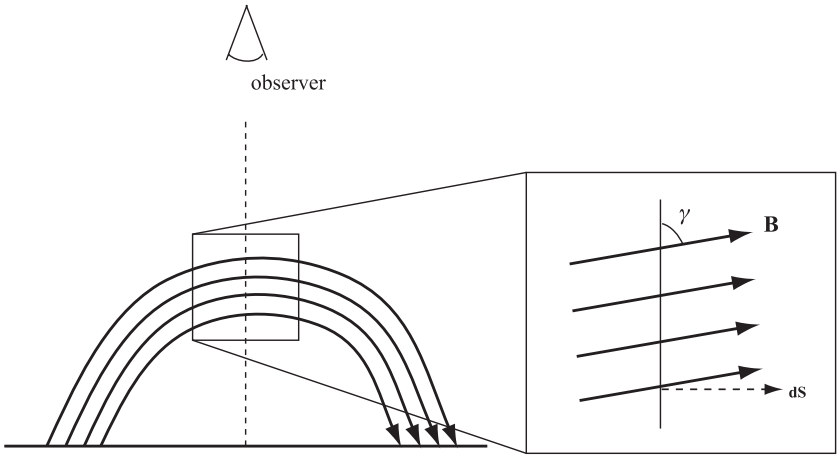

Figure 9. Representation of the vector field and the surface used for the definition of the horizontal magnetic flux.

Stokes V signal is detected, the retrieved inclinations indicate that the field lines are more vertical. The retrieved inclinations nicely delineate the shape of the flux tube.

6.2. LOS Velocity Topology

The distributions of LOS velocity along the axis of the flux tube can be seen in Figure 8 (middle panels). Since the plasma velocity depends on whether the pixel is located in the granular/intergranular region, the normalized continuum intensities are also displayed in the bottom panels of Figure 8.

Pixels 1–4 and 1–5 have continuum intensities lower than 1.0, and correspond to the edge of the granule (also see Figure 1). In these pixels, the flux tube shows downward motion. In the same pixel, the background atmosphere shows larger downflows. From pixel 1–10 to pixel 1–12, the continuum intensity is above 1.0 and becomes larger. These pixels correspond to the transition region from the edge of the granular cell to the interior of the granule. There, the flux tube exhibits a strong upward motion, with velocities reaching 2.7 km s^{-1}. In contrast, the background plasma above the flux tube is slightly redshifted with LOS velocities smaller than 1 km s^{-1}. Note that the absolute

Doppler velocities with respect to the solar surface are shown in Figure 8. Borrero & Bellot Rubio (2002) obtained a two-component model of the solar photosphere from the inversion of spatially and temporally averaged solar intensity profiles, and they found upflows of $\sim$1.1 km s^{-1} in granular cells at around $\log\tau \sim -0.3$ (note that they only correct the gravitational redshift). Thus, the upward velocities of the flux tube we find in our analysis are larger than that for typical granular cells.

In the second scan, the flux tube is located higher in the atmosphere. At the apex of the loop (pixel 2–13), the continuum intensity is slightly below 1.0. This pixel appears to be located at the boundary between the granule and the intergranular lane. The pixels around the apex of the flux tube show upward velocities reaching $\sim$ 3 km s^{-1}, clearly indicating the rising motion of the flux tube.

Next, we examine the more vertical portion of the flux tube located in the low atmosphere. The region of negative polarity (pixels 2–17, 2–24, 2–25, and 2–26) shows the continuum intensities larger than 1.0, corresponding to the inner part of the granule. There, the flux tube has strong upward velocities ranging from $\sim$2 km s^{-1} to $\sim$ 4 km s^{-1}. These velocity values are larger than that of the typical upflows observed in granules.

In the portion of the flux tube with positive polarity (pixels 2–3 and 2–4), the continuum intensity is lower than 1.0. These pixels are located in an intergranular lane. The flux tube at these positions has a downward motion ranging from $\sim$2.3 km s^{-1} to $\sim$4.6 km s^{-1} at $-0.5 < \log\tau < 0$. Typical downflow velocities in the intergranular lanes in the lower photosphere ($-0.5 < \log\tau < 0$) are between 2.2 km s^{-1} and 3.7 km s^{-1} (Borrero & Bellot Rubio 2002) comparable to what we measured. Therefore, the downward motion of the flux tube may be driven by the convective motion so that the flux tube may be forced to be submerged with the downward flow field.

As we have seen, the flux tube is located at around $\log\tau = 0$ in the first scan ($\Delta t = 0$ s), while in the second scan ($\Delta t =$ 130 s), the center of the flux tube is located at around $\log\tau = -1.7$. This clearly indicates that the flux tube goes upward and reaches higher photospheric layers with time. The geometrical distance between $\log\tau = 0$ and $\log\tau = -1.7$ is around 244 km. Given the time difference of 130 s between these two scans, the rise velocity of the flux tube is 1.9 km s^{-1}. This is consistent with the inferred upward motion of 2 km s^{-1} for the flux tube (see middle panels of Figure 8).

6.3. Cross-sectional Shape of Flux Tube

To estimate the width of the flux tube, we need to find a pixel, where the 1σ confidence regions in the χ^2 maps (marked by the yellow contour in Figures 6 and 7) are not elongated and where we observe both the upper and lower boundaries of the flux tube. In the second scan, the center of the analyzed THMF is already too high for our purpose. We select pixel 2–16. This pixel is located at the center of the THMF, and its χ^2 1σ confidence levels are not spanning over a wide range of $G_{\rm width}$ and $G_{\rm pos}$. The upper and the lower boundary are within the line-forming region, as well (see the top right panel of Figure 8).

For pixel 2–16, the position of the flux tube is located at $\log\tau = -1.4$ and the width corresponds to 0.8 in $\log\tau$ units as given by the $\chi^2_{\rm min}$. We define the radius of the flux tube along the LOS as the FWHM of the Gaussian function that represents it. In this case, the vertical extension of the flux tube is around 190 km. We estimate the horizontal size to be approximately 360 km, since the THMF occupies three pixels (2–9, 2–16, and 2–22) at around the location of pixel 2–16. It should be kept in mind that the real horizontal size might be larger since a weaker Stokes Q and U signal can be observed surrounding the THMF. The discrepancy between the vertical and horizontal size of the flux tube indicates that the flux tube is squeezed in the vertical direction.

6.4. Total Magnetic Flux Carried by THMF

In this section, we estimate the magnetic flux Φ_H carried by the THMF, since we know the vertical (along the LOS) and lateral cross section of the flux tubes as shown in the previous sections. Let $\vec{B}(z)$ be the magnetic field vector with inclination $\gamma(z)$, z being the geometrical height, and the SOT/SP pixel size l' of about 120 km. The per-pixel magnetic flux φ_h through the surface $\vec{S}$ (see Figure 9) is given by

$$\varphi_h = \int_S \vec{B}\cdot d\vec{S} \approx \int_{z_0(\log\tau=0)}^{z_1(\log\tau=-2.5)} B(z)\cos(90^\circ-\gamma(z))(l'dz). \quad (3)$$

The integration range is set to cover the line-forming region of the Fe I lines. To estimate the total magnetic flux Φ_H carried by the THMF, we sum up the φ_h values for pixels of 2–1, 2–7, 2–14, and 2–20 from the second scan. The total magnetic flux Φ_H turns out to be 3.1×10^{17} Mx. This value is in agreement with that derived by Jin et al. (2009), who assumed that the vertical extent of the flux tubes is the same as that of the scale height of 100 km. In our analysis, we resolve the vertical structure of the magnetic flux tube using SIRGAUS. This has allowed us to derive the magnetic flux more directly. Note that the total magnetic flux may be different depending on the polarization threshold used in the analysis, so that our magnetic flux estimate represents a lower limit.

7. SUMMARY AND DISCUSSIONS

7.1. Three-dimensional Magnetic Structure and Evolution

We have analyzed a magnetic phenomenon in which a horizontal magnetic field patch appears first at the edge of a granular cell at $\Delta t = 0$ s. Later at $\Delta t = 130$ s, the size of the patch harboring horizontal fields becomes larger, and vertical magnetic fields with opposite polarity appear at both ends of the magnetic patch. Then (at $\Delta t = 260$ s), the horizontal magnetic field disappears, while the vertical magnetic fields remain and separate. The whole process takes about 4 minutes. This event corresponds to a typical example of the so-called THMF.

We have successfully applied the SIRGAUS inversion code to this event and analyzed its three-dimensional magnetic structure. The results show that the flux tube occupies only a fraction of the line formation region of the Fe I lines at 630.2 nm and that it has an upward movement. The magnetic flux tube rises from $\log\tau \sim 0$ (0 km) to $\log\tau \sim -1.7$ (244 km) between the first and the second scan that are separated in time by 130 s. The Doppler velocity of the flux tube consistently indicates the upward motion. The magnetic field strength of the flux tube is about 400 G. The azimuth direction of the magnetic field is aligned with the axis of the flux tube, and the flux tube does not show any helical structure.

So far, to determine whether the observed magnetic loops correspond to the rising Ω loops or to submerging U loops, Doppler velocity measurement have been used (e.g., Martínez González & Bellot Rubio 2009). Our analysis with SIRGAUS

presented here shows that the flux tube with shallow but clear Ω shape rises. We observe only a small part of the shallow Ω loop above the continuum formation layer and this might be just a part of a larger-scale magnetic structure located in the bulk of the convection zone.

7.2. Force Balance of Flux Tube

The field strength of the flux tube is ∼400 G in the first scan ($\Delta t = 0$ s). Taking the velocity of the convective flow to be $v = 2 \times 10^5$ cm s^{-1} and the mean density at the base of the photosphere ($\log \tau \sim 0$) to be $\rho = 2.7 \times 10^{-7}$ g cm^{-3}, we find that the equipartition field strength is $B_{\rm eq} = (4\pi\rho)^{1/2} v = 370$ G. Therefore, the inferred field strengths are comparable to $B_{\rm eq}$. This is consistent with the fact that the flux tube seems to maintain its integrity during its rise from the lower photosphere upwards.

In this section, we compare the buoyancy force, $F_b = (\rho_e - \rho_i)g$, with the magnetic tension force, $F_T = B^2/4\pi L$, acting on the flux tube at $\Delta t = 130$ s. Here, ρ_i and ρ_e are the plasma densities inside and outside the flux tube, respectively, g is the gravity acceleration of 2.7×10^4 cm s^{-2}, and L is the curvature radius of the Ω loop. Here, we use all the plasma parameters (temperature, field strength, and the density) at the height where the flux tube is located and the three-dimensional geometrical scale of the flux tube (the length and the cross section). From the separation of the footpoints in the second scan (which is about 1320 km) and from the averaged magnetic field inclination in the footpoints (about 47°), we estimate L to be 1250 km. The comparison is made at the apex of the flux tube which is located above $\log \tau \sim -1.0$. There, the temperature T is ∼4950 K (corresponding to the averaged value from $\log \tau = -1.0$ to -2.0 at pixel 2–14). Assuming that the temperature is the same inside and outside of the flux tube, F_b can be written as $F_b = \frac{B^2}{8\pi} \cdot \frac{m_p g}{2k_{\rm B}T}$, where m_p is the proton mass, and $k_{\rm B}$ the Boltzmann constant. The ratio between F_b and F_T is then $\frac{F_b}{F_T} = \frac{m_p g L}{4k_{\rm B}T} \sim 2$. This clearly indicates that the buoyancy force, F_b, participates in the emergence process of the magnetic flux tube.

If we suppose that the stationary state is reached, then the buoyancy force, the magnetic tension force, and the resultant drag force associated with the rising motion are balanced:

$$\begin{aligned}(\rho_e - \rho_i)g \cdot al - \frac{B^2}{4\pi L} \cdot al - 0.5 C_d \rho_e u^2 l \\ = \frac{B^2}{8\pi} \cdot \frac{m_p g}{2k_{\rm B}T} \cdot al - \frac{B^2}{4\pi L} \cdot al - 0.5 C_d \rho_e u^2 l \\ = 0. \end{aligned} \quad (4)$$

With C_d being the aerodynamic coefficient of the order of unity (Parker 1979), and u the relative velocity of the flux tube with respect to the velocity of the surrounding plasma, a and l are the vertical extent and the horizontal size of the flux tube, respectively. We take ρ_e to be 7.78×10^{-8} g cm^{-3} (corresponding to the mean density from $\log \tau = -1.0$ to -2.0 at pixel 2–14). The relative velocity u obtained from Equation (4) is then 2.3 km s^{-1}, which is consistent with the observed relative Doppler velocity associated to the flux tube.

As shown in Section 6.3, the vertical extent of the flux tube ($a = 190$ km) is smaller than its lateral size ($l = 360$ km). Therefore, the cross section of the flux tube has a flattened shape. Magara (2001) studied the emergence of large flux tubes with larger field strengths which form active regions. He found that the top of the loop decelerates when it reaches photospheric layers, while the bottom of the flux tube continues to rise. The reason is that the photosphere is a convectively stable layer. Therefore, the cross section of the tube changes from the circular shape to horizontally extended shape. The same process may take place for granular-sized magnetic flux tubes. Steiner et al. (2008) pointed out that an emerging flux tube can get pushed to the middle and upper photosphere by overshooting convection, forming atmospheric layers full of horizontal fields. This may also contribute to the flattening of the flux tube.

7.3. Magnetic Flux and Energy

The horizontal magnetic flux Φ_H is estimated to be 3.1×10^{17} Mx near the apex of the flux tube. Recently, Ishikawa & Tsuneta (2009a) reported that the occurrence rate of THMFs is about 1.1×10^{-10} km^{-2} s^{-1} in a quiet Sun region. Also, Tsuneta et al. (2008b) and Ito et al. (2010) have shown the presence of horizontal magnetic fields ubiquitously in the polar region, and that there is no difference in the intrinsic magnetic field strengths between the quiet Sun and the polar region. Lites (2009) suggested that the uniform fluctuations of longitudinal magnetogram signals over the whole disk observed by Harvey et al. (2007) are the same phenomenon as the horizontal fields observed by *Hinode*. All these results together indicate that THMFs would have the same occurrence rate all over the solar surface. Combining these observations, we conclude that THMFs could carry a total magnetic flux of 1.8×10^{25} Mx per day to the higher atmosphere which corresponds to a total of 7×10^{28} Mx in one solar cycle (11 years). This estimation is based on the assumption that all THMFs reach higher atmospheric layers and that all of them carry the same amount of magnetic flux Φ_H (given in this paper). Although our calculations are based only upon a single event, similar values have also been found by Jin et al. (2009) and Martínez González & Bellot Rubio (2009). The magnetic flux carried by THMFs is much larger than the total magnetic flux in sunspot regions during one solar cycle which corresponds to about 10^{25} Mx (Harvey 1993).

Ishikawa & Tsuneta (2009a) have estimated the magnetic energy flux carried by THMFs, and found that the amount of energy flux is comparable to the total chromospheric and coronal energy loss, assuming that all THMFs reach above the photosphere. In order to perform a more precise estimation of the total magnetic flux and the total magnetic energy that THMFs could carry to higher atmospheric layers, we need to know what percentage of THMFs reach the chromosphere or higher layers in addition to the precise estimation of the magnetic flux of each THMF. Such statistical analysis was done by Martínez González & Bellot Rubio (2009), who pointed out that 23% of the horizontal fields that emerge with clear bipolar footpoints in the photosphere reach the low chromosphere.

7.4. Disappearance of THMFs

We show that the THMF analyzed in this paper is rising through the line-forming layer of the Fe I 630.2 nm lines and that it reaches higher atmospheric layers. The flux tube essentially maintains its integrity during the rising motion. At the beginning of this paper, we addressed three different possibilities of the THMF's disappearance. The observed event is clearly into the third of the suggested mechanisms, i.e., the THMF goes through the photosphere reaching the layers above the line-forming region of Fe I 630.2 nm lines. Some THMFs do not show

any conspicuous footpoints in their lifetime (Ishikawa et al. 2008; Jin et al. 2009). Such THMFs possibly harbor weaker magnetic fields than the equipartition field strength. Thus, the convective motion may destroy the flux tube before it reaches the upper photosphere, or it may force it to submerge below the photosphere.

The authors want to express their sincere appreciation to Bellot Rubio for his pioneering work, and thank him for allowing us to use the SIRGAUS software. The authors are thankful for the encouragement by Bellot Rubio, Ruiz Cobo, Del Toro Iniesta, and Orozco Suárez.

Hinode is a Japanese mission developed and launched by ISAS/JAXA, with NAOJ as a domestic partner and NASA and STFC (UK) as international partners. It is operated by these agencies in co-operation with ESA and NSC (Norway). The financial support from GA AS CR IAA 300030808 to Jan Jurčák is gratefully acknowledged.

REFERENCES

Abbett, W. P. 2007, ApJ, 665, 1469
Allende Prieto, C., & Garcia Lopez, R. J. 1998, A&AS, 129, 41
Beckers, J. M., Bridges, C. A., & Gilliam, L. B. 1976, in A High Resolution Spectral Atlas of the Solar Irradiance from 380 to 700 nanometers. Vol. 2: Graphical Form (Hanscom, MA: Air Force Geophys. Lab)
Bellot Rubio, L. R. 2003, in ASP Conf. Ser. 307, Solar Polarization, ed. J. Trujillo-Bueno & J. Sanchez Almeida (San Francisco, CA: ASP), 301
Borrero, J. M., & Bellot Rubio, L. R. 2002, A&A, 385, 1056
Cabrera Solana, D., Bellot Rubio, L. R., & del Toro Iniesta, J. C. 2005, A&A, 439, 687
Centeno, R., et al. 2007, ApJ, 666, L137
Del Toro Iniesta, J. C. 2003, Introduction to Spectropolarimetry (Cambridge: Cambridge Univ. Press)
Del Toro Iniesta, J. C., & Ruiz Cobo, B. 1996, Sol. Phys., 164, 169
De Pontieu, B. 2002, ApJ, 569, 474
Gömöry, P., et al. 2010, A&A, 511, 14
Harvey, J. W., Branston, D., Henney, C. J., & Keller, C. U. 2007, ApJ, 659, L177
Harvey, K. L. 1993, PhD thesis, Univ. Utrecht
Ichimoto, K., et al. 2008, Sol. Phys., 249, 233
Ishikawa, R., & Tsuneta, S. 2009a, A&A, 495, 607
Ishikawa, R., & Tsuneta, S. 2009b, in ASP Conf. Ser. 415, The Second *Hinode* Science Meeting: Beyond Discovery—Toward Understanding, ed. B. Lites et al. (San Francisco, CA: ASP), 132
Ishikawa, R., et al. 2008, A&A, 481, L25
Isobe, H., Proctor, M. R. E., & Weiss, N. O. 2008, ApJ, 679, L57
Ito, H., Tsuneta, S., Shiota, D., Tokumaru, M., & Fukui, K. 2010, ApJ, submitted
Jin, C., Wang, J., & Zhou, G. 2009, ApJ, 697, 693
Jurčák, J., et al. 2007, PASJ, 59, 601
Kosugi, T., et al. 2007, Sol. Phys., 243, 3
Lites, B. W. 2009, ScChG, 52, 1660
Lites, B. W., Leka, K. D., Skumanich, A., Martinez Pillet, V., & Shimizu, T. 1996, ApJ, 460, 1019
Lites, B. W., et al. 2008, ApJ, 672, 1237
Magara, T. 2001, ApJ, 549, 608
Martínez González, M. J., & Bellot Rubio, L. R. 2009, ApJ, 700, 1391
Martínez González, M. J., Collados, M., Ruiz Cobo, B., & Solanki, S. K. 2007, A&A, 469, L39
Orozco Suárez, D., et al. 2007a, ApJ, 670, L61
Orozco Suárez, D., et al. 2007b, PASJ, 59, 837
Parker, E. N. 1979, Cosmical Magnetic Fields: Their Origin and Their Activity (Oxford: Clarendon)
Press, W. H., Teukolsky, S. A., Vetterling, W. T., & Flannery, B. P. 2007, Numerical Recipes : The Art of Scientific Computing (Cambridge: Cambridge Univ. Press), 812
Ruiz Cobo, B., & del Toro Iniesta, J. C. 1992, ApJ, 398, 375
Ruiz Cobo, B., & del Toro Iniesta, J. C. 1994, A&A, 283, 129
Sanchez Almeida, J., & Lites, B. W. 1992, ApJ, 398, 359
Schüssler, M., & Vögler, A. 2008, A&A, 481, L5
Shimizu, T., et al. 2008, Sol. Phys., 249, 221
Solanki, S. K., & Pahlke, K. D. 1988, A&A, 201, 143
Steiner, O., Rezaei, R., Schaffenberger, W., & Wedemeyer-Böhm, S. 2008, ApJ, 680, L85
Suematsu, Y., et al. 2008, Sol. Phys., 249, 197
Tsuneta, S., et al. 2008a, Sol. Phys., 249, 167
Tsuneta, S., et al. 2008b, ApJ, 688, 1374
Vögler, A., & Schüssler, M. 2007, A&A, 465, L43